Radially symmetric solutions of the ultra-relativistic Euler equations in several space dimensions

Matthias Kunik [a], Adrian Kolb [b], Siegfried Müller [b], Ferdinand Thein [b,c,*,1]

[a] *Otto-von-Guericke-Universität Magdeburg, Institut für Analysis und Numerik, Universitätsplatz 2, D-39106 Magdeburg, Germany*
[b] *RWTH Aachen University, Institut für Geometrie und Praktische Mathematik, Templergraben 55, D-52056 Aachen, Germany*
[c] *Johannes Gutenberg-Universität Mainz, Staudingerweg 9, D-55128 Mainz, Germany*

ARTICLE INFO

ABSTRACT

The ultra-relativistic Euler equations for an ideal gas are described in terms of the pressure, the spatial part of the dimensionless four-velocity and the particle density. Radially symmetric solutions of these equations are studied in two and three space dimensions. Of particular interest in the solutions are the formation of shock waves and a pressure blow up. For the investigation of these phenomena we develop a one-dimensional scheme using radial symmetry and integral conservation laws. We compare the numerical results with solutions of multi-dimensional high-order numerical schemes for general initial data in two space dimensions. The presented test cases and results may serve as interesting benchmark tests for multi-dimensional solvers.

1. Introduction

In this paper we focus on radially symmetric solutions of a special relativistic system which is much simpler than flows in general relativistic theory. Interestingly, even compared to the classical Euler equations of non-relativistic gas dynamics the equations we consider exhibit a simpler mathematical structure.

We are concerned with the ultra-relativistic equations for a perfect fluid in Minkowski space-time $\mathbf{x} = (x_1, x_2, x_3)$, $t = x_0$, namely

$$\sum_{\beta=0}^{3} \frac{\partial T_{\alpha\beta}}{\partial x_\beta} = 0 \tag{1.1}$$

with $\alpha, \beta \in \{0, 1, 2, 3\}$ and the energy-momentum tensor

$$T_{\alpha\beta} = -\tilde{p} g_{\alpha\beta} + 4\tilde{p} u_\alpha u_\beta \tag{1.2}$$

for the ideal ultra-relativistic gas. Here $\tilde{p}$ represents the pressure, $\mathbf{u} \in \mathbb{R}^3$ is the spatial part of the four-velocity vector $(u_0, u_1, u_2, u_3) = (\sqrt{1 + |\mathbf{u}|^2}, \mathbf{u})$. For the ideal ultra-relativistic gas the thermal energy dominates and thus the local energy density e at rest is linked to the pressure $\tilde{p}$ by

$$e = 3\tilde{p}. \tag{1.3}$$

Note that (1.3) is universal for an ideal gas in the ultra-relativistic regime. We exemplarily refer to Lai [18], where a polytropic gas is considered in the relativistic case. For works using the Synge energy in the relativistic setting we refer to Ruggeri and Sugiyama [20] and references therein. In both cases the equations of state simplify to (1.3) in the ultra-relativistic limit. The flat Minkowski metric is given as

$$g_{\alpha\beta} = \begin{cases} +1, & \alpha = \beta = 0, \\ -1, & \alpha = \beta = 1, 2, 3, \\ 0, & \alpha \neq \beta. \end{cases} \tag{1.4}$$

We note that the quantities u_α, $T_{\alpha\beta}$, $g_{\alpha\beta}$ and even x_α are usually written as Lorentz-invariant tensors with *upper indices* instead of lower indices in order to make use of Einstein's summation convention. But in the following calculations these upper indices could be mixed up with powers. Since we will not make use of the lowering and raising of Lorentz-tensor indices, our change of the notation will not lead to confusions. For the physical background we refer to Weinberg [21, Part I, pp 47-52], further details can be found in Kunik [13, Chapter 3.9] and for the corresponding classical Euler equations see Courant and Friedrichs [5]. For a general introduction to the mathematical theory of hyperbolic conservation laws see Bressan [3] and Dafermos [6]. An overview of radially symmetric solutions to conservation laws is given in the survey paper by Jenssen [12]. Previous results on the numerical treatment of the ultra-relativistic Euler equations are given in Abdelrahman et al. [2] proposing a front tracking scheme and for kinetic schemes we cite Kunik et al. [15–17]. For a recent treatment of the ultra-relativistic equations, especially in the context of symmetric hyperbolic systems, we refer to Freistühler [7], Ruggeri and Sugiyama [20] and the references therein. In Kunik et al. [14] the ultra-relativistic Euler equations are studied and a one-dimensional radially symmetric solver that can provide non-trivial reference solutions for genuinely three-dimensional calculations is developed. In the present paper we provide a one-dimensional radially symmetric solver called RadSymS which may provide benchmark tests for the validation of the corresponding two-dimensional solvers. Interestingly, the solver RadSymS can be obtained only by a modification of the routine "Euler" described in [14, Thm. 4.3, Def. 4.4]. This analogy was not clear a priori, and in order to keep our paper self-contained, we describe the complete construction of RadSymS. In this way we finally obtain a unified presentation of the multi-dimensional theory in the paper at hand. The outline of the remaining paper is as follows. In Section 2 we present the equations subject of study in this work. In Section 3 the one–dimensional scheme to compute the radially symmetric solutions is given. In Section 4 we first validate the one-dimensional scheme in case of self-similar solutions where we compare with solutions of an ODE system. We further present three additional radially symmetric benchmark problems without scale invariance. With these examples we verify that the one-dimensional solver can be used to validate genuinely multi-dimensional solvers. A conclusion is given in Section 5. For the readers convenience we also provide the eigenstructure of the system under consideration in Appendix B which, to the best of our knowledge, cannot be found in the literature.

2. Conservative formulations of the equations

In the following we introduce two kinds of conservative formulations of (1.1). First, the multi-dimensional form of the ultra-relativistic Euler equations and second the conservative radially symmetric form. In both cases we consider either $d = 2$ or $d = 3$ space dimensions. Then the unknown quantities $\tilde{p}$ and $\mathbf{u} = (u_1, \ldots, u_d) \in \mathbb{R}^d$ satisfying (1.1) depend on time $t \geq 0$ and position $\mathbf{x} = (x_1, \ldots, x_d) \in \mathbb{R}^d$.

Putting $\alpha = 0$ in (1.1) gives the conservation of energy

$$\frac{\partial}{\partial t}\left(3\tilde{p} + 4\tilde{p}|\mathbf{u}|^2\right) + \sum_{k=1}^{d} \frac{\partial}{\partial x_k}\left(4\tilde{p}u_k\sqrt{1 + |\mathbf{u}|^2}\right) = 0, \tag{2.1}$$

whereas for $\alpha = j = 1, \ldots, d$ we obtain the conservation of momentum

$$\frac{\partial}{\partial t}\left(4\tilde{p}u_j\sqrt{1 + |\mathbf{u}|^2}\right) + \sum_{k=1}^{d} \frac{\partial}{\partial x_k}\left(\tilde{p}\delta_{jk} + 4\tilde{p}u_ju_k\right) = 0, \quad j = 1, \ldots, d. \tag{2.2}$$

In this paper, we study radially symmetric solutions and construct corresponding schemes to solve the ultra-relativistic Euler equations (2.1), (2.2) in two and three space dimensions. Here we focus on the case $d = 2$, since a detailed treatment of the case $d = 3$ is presented in [14, Sec. 2, Eqn. (2.5)]. For completeness we give a summary of the radially symmetric equations for $d = 2, 3$ in (4.1) in the present paper.

Assume for a moment a smooth solution $\tilde{p}, \mathbf{u}$ of the ultra-relativistic Euler equations (2.1), (2.2). We put $r = |\mathbf{x}|$ for $r > 0$ and look for radially symmetric solutions

$$p = p(t, r) = \tilde{p}(t, \mathbf{x}) > 0, \quad \mathbf{u}(t, \mathbf{x}) = \frac{u(t, r)}{r}\mathbf{x}. \tag{2.3}$$

Here the quantity $\mathbf{u}(t,\mathbf{x}) \in \mathbb{R}^2$ is completely determined by a new *real-valued quantity* $u(t,r)$ depending on $t > 0$, $r > 0$. For continuity we have the boundary condition

$$\lim_{r \searrow 0} u(t,r) = 0, \quad t > 0. \tag{2.4}$$

Note that $\mathbf{n} = \frac{1}{r}\mathbf{x}$ is the outer normal vector field of the circle $\partial \mathcal{B}_R$ bounding the ball

$$\mathcal{B}_R = \{\mathbf{x} \in \mathbb{R}^2 \,:\, |\mathbf{x}| \le R\}$$

of radius $R > 0$ and that $|\mathbf{u}|^2 = u^2$ as well as $u = \mathbf{u} \cdot \mathbf{n}$. Therefore, it is natural to apply the Gaussian divergence theorem for the integration of the divergence term in (2.1) over $\mathcal{B}_R$ to make use of the radial symmetry of the solutions. We obtain with (2.3) for any fixed $R > 0$

$$2\pi \frac{\partial}{\partial t} \int_0^R \left(3p(t,r) + 4p(t,r)u^2(t,r)\right) r\,dr + \int_{\partial \mathcal{B}_R} 4pu\sqrt{1+u^2}\,ds = 0.$$

The contour integral with the differential length ds on the right-hand side is constant. Hence we have

$$\frac{\partial}{\partial t} \int_0^R \left(3p(t,r) + 4p(t,r)u^2(t,r)\right) r\,dr + 4p(t,R)u(t,R)R\sqrt{1+u^2(t,R)} = 0. \tag{2.5}$$

This idea does not work for the momentum equation (2.2), because (2.3) would give zero after integration over $\mathcal{B}_R$. Here we integrate (2.2) for $j = 2$ over the upper half-ball

$$\mathcal{B}_R^+ = \{\mathbf{x} = (x_1, x_2) \in \mathbb{R}^2 \,:\, x_2 \ge 0\},$$

use the Gaussian divergence theorem and polar coordinates

$$x_1 = r\cos\varphi, \; x_2 = r\sin\varphi$$

with $0 < r < R$ and $0 < \varphi < \pi$ and obtain with (2.3)

$$2\frac{\partial}{\partial t} \int_0^R 4p(t,r)u(t,r)r\sqrt{1+u^2(t,r)}\,dr + 2R\left(4p(t,R)u^2(t,R) + p(t,R)\right) - 2\int_0^R p(t,r)dr = 0. \tag{2.6}$$

Now we differentiate the Eqns. (2.5), (2.6) with respect to $R > 0$. Afterwards we replace R by the better suited variable $x > 0$.

We put $p = p(t,x)$, $u = u(t,x)$ for abbreviation and have the 2 by 2 system

$$\begin{cases} \dfrac{\partial}{\partial t}\left(xp(3+4u^2)\right) + \dfrac{\partial}{\partial x}\left(4xpu\sqrt{1+u^2}\right) &= 0, \\[2mm] \dfrac{\partial}{\partial t}\left(4xpu\sqrt{1+u^2}\right) + \dfrac{\partial}{\partial x}\left(xp(1+4u^2)\right) &= p. \end{cases} \tag{2.7}$$

The validity of this system may also be checked by differentiation from (2.1), (2.2) and (2.3). The solutions of (2.7) are restricted to the state space $\mathcal{S}_{eul} = \{(p,u) \in \mathbb{R}^2 \,:\, p > 0\}$.

It is well-known that even for smooth initial data, where the fields are prescribed at $t = 0$, the solution may develop shock discontinuities. This requires a weak form of the conservation laws in (2.7).

For the formulation of weak solutions we first introduce a transformation in state space. With

$$\tilde{\mathcal{S}}_{eul} = \{(a,b) \in \mathbb{R}^2 \,:\, |b| < a\}$$

there is a one-to-one transformation $\Theta : \mathcal{S}_{eul} \mapsto \tilde{\mathcal{S}}_{eul}$ given by

$$\Theta(p,u) = \begin{pmatrix} p(3+4u^2) \\ 4pu\sqrt{1+u^2} \end{pmatrix} = \begin{pmatrix} a \\ b \end{pmatrix}. \tag{2.8}$$

The inverse transformation is given by

$$p = \frac{1}{3}\left(\sqrt{4a^2 - 3b^2} - a\right), \quad u = \frac{b}{\sqrt{4p(p+a)}}. \tag{2.9}$$

In [13] we have used contour integrals for weak solutions of conservation laws, following Oleinik's formulation [19] for a scalar conservation law. We put

$$c = c(a,b) = \frac{5}{3}a - \frac{2}{3}\sqrt{4a^2 - 3b^2}, \tag{2.10}$$

and obtain especially for a smooth solution a, b and for each convex domain $\Omega \subset Q$ with piecewise smooth boundary $\partial\Omega \subset Q$:

$$\int_{\partial\Omega} xa\,dx - xb\,dt = 0, \quad \int_{\partial\Omega} xb\,dx - xc\,dt = \frac{1}{2}\iint_\Omega (a-c)\,dt\,dx. \tag{2.11}$$

This is a proper weak formulation which will be used next for more general piecewise smooth solutions. Using the transformation in state space (2.8) we obtain an initial value problem for a and b. In the quarter plane $t > 0$, $x > 0$ we have to require that $|b(t,x)| < a(t,x)$. Then we prescribe for $x > 0$ the *two initial functions*

$$\lim_{t \searrow 0} a(t,x) = a_0(x), \quad \lim_{t \searrow 0} b(t,x) = b_0(x), \ x > 0 \tag{2.12}$$

with $|b_0(x)| < a_0(x)$ for $x > 0$.

In the presence of shock waves we also obtain a very simple characterization of the entropy condition, see [1, Chapter 2.1] for more details: If for $p_-, p_+ > 0$ the left state (p_-, u_-) can be connected to the right state (p_+, u_+) by a single shock satisfying the Rankine-Hugoniot jump conditions, then this shock wave satisfies the correct entropy condition if and only if $u_- > u_+$. This condition can also be checked easily for our numerical solutions with shock curves.

In Section 3 the conservation laws (2.11) are used in order to develop a one–dimensional numerical scheme to compute the radially symmetric solutions of the system (2.1), (2.2) in two space dimensions. Compared to the corresponding scheme for $d = 3$ presented in [14] it turns out that both schemes have essentially the same structure. To be more precise, for $d = 2$ only the subroutine "Euler" defined in Definition 3.4 is slightly modified.

3. Formulation of a numerical scheme for the radially symmetric solutions

We develop a one-dimensional numerical scheme for the initial value problem of the radially symmetric ultra-relativistic Euler equations in two space dimensions. As mentioned earlier the details for the three-dimensional case can be found in [14]. We show that our scheme preserves positive pressure. The method of contour-integration for the formulation of the balance laws (2.11) is used to construct a function called "Euler". This function enables us to obtain the time evolution of the numerical solution on a staggered grid. More precisely it allows us to construct the solution (a', b') at the next time step from the solution $(a_\pm, b_\pm)$ in two neighboring grid points at the previous time step according to Fig. 2. Parts of the construction are exactly the same as in [14, Section 4], namely the determination of the grid points. It finally turns out that only the routine "Euler" has to be modified for the solution of the two-dimensional model. For the sake of a better understanding we now present the detailed construction. First we determine the computational domain and define some quantities which are needed for its discretization.

1) Given are $t_*, x_* > 0$ in order to calculate a numerical solution of the initial value problem (2.11), (2.12) in the time range $[0, t_*]$ and the spatial range $[0, x_*]$.

2) We want to use a staggered grid scheme. Any given number $N \in \mathbb{N}$ with $N \cdot x_* \geq t_*$ determines the time step size

$$\Delta t = \frac{t_*}{2N}.$$

The time steps are

$$t_n = (n-1)\Delta t, \quad n = 1, \ldots, 2N+1.$$

3) Put

$$M = \left\lfloor \frac{x_*}{t_*} N \right\rfloor \geq 1,$$

then the spatial mesh size is

$$\Delta x = \frac{x_*}{M},$$

with the spatial grid points

$$x_j = (j-1)\Delta x, \quad j = 1, \ldots, N+M+1.$$

Note that our scheme uses a trapezoidal computational domain $\mathcal{D}$ defined below that includes the target domain $[0, t_*] \times [0, x_*]$. Thereby, we can use all initial data that influence the solution on the target domain. In this way we avoid using a numerical boundary condition at x_*.

4) The number

$$\lambda = \frac{\Delta x}{2\Delta t} \geq 1$$

is used to satisfy the CFL-condition and to define the computational domain $\mathcal{D} = \left\{(t,x) \in \mathbb{R}^2 \ : \ 0 \leq t \leq t_*, \quad 0 \leq x \leq x_* + \lambda(t_* - t)\right\}$.

The typical trapezoidal form of the computational domain is illustrated in Fig. 1. For the formulation and the stability of our numerical
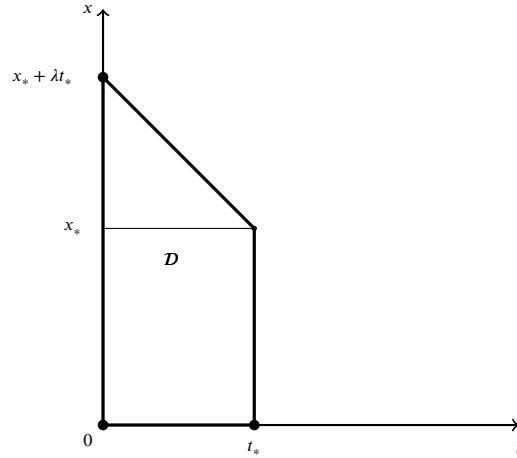
Fig. 1. The computational domain $\mathcal{D}$.

scheme we need two lemmas, given in [14, Lemma 4.1] and [14, Lemma 4.2].

Lemma 3.1. *Assume that $|b_\pm| < a_\pm$ and put $c_\pm = c(a_\pm, b_\pm)$ according to (2.10). We recall that $\lambda \geq 1$. Then*

a) $-\left(a_- + \dfrac{b_-}{\lambda}\right) < b_- + \dfrac{c_-}{\lambda} < a_- + \dfrac{b_-}{\lambda},$

b) $-\left(a_+ - \dfrac{b_+}{\lambda}\right) < b_+ - \dfrac{c_+}{\lambda} < a_+ - \dfrac{b_+}{\lambda}.$

Lemma 3.2. *Assume that $a > 0$, $0 < \eta \leq 1/3$ and $-a(1 + \eta) < \xi < a(1 - \eta)$. Then we obtain $4a^2(1 + 3\eta^2) - 3\xi^2 > 0$ and*

$$\left| \frac{\xi + \eta \sqrt{4a^2(1 + 3\eta^2) - 3\xi^2}}{1 + 3\eta^2} \right| < a.$$

For the numerical discretization of the integral balance laws (2.11) we choose the triangular balance domain Ω depicted in Fig. 2. We assume that the midpoints $P_- = (\bar{t}, \bar{x} - \Delta x/2)$, $P_+ = (\bar{t}, \bar{x} + \Delta x/2)$ and $P' = (\bar{t} + \Delta t, \bar{x})$ of the cords of $\partial\Omega$ are numerical grid points for the computational domain $\mathcal{D}$. Let the numerical solution $(a_\pm, b_\pm)$ be given at the grid points $P_\pm$. We have to require $|b_\pm| < a_\pm$ for the numerical solution in the actual time step $\bar{t} = t_n$ with $n = 1, \ldots, 2N$. The major task is to calculate the numerical solution (a', b') for the next time step $\bar{t} + \Delta t = t_{n+1}$ at its grid point P', see Fig. 2. The spatial value $\bar{x} \geq 0$ is given. We have to determine a function

$$\text{Euler}(a_-, b_-, a_+, b_+, \bar{x}, \Delta x, \lambda) = (a', b') \tag{3.1}$$

for the calculation of (a', b'). This leads to the structure of a staggered grid scheme. Note that at the boundary the balance region Ω may have parts outside $\mathcal{D}$, e.g. points below the half-space $x \geq 0$. In the latter case we employ a simple reflection principle for the numerical solution in order to use the function Euler as well for the boundary points with $\bar{x} = 0$.

Next we make use of the fact that the points $P_\pm$ with the numerical values $(a_\pm, b_\pm)$ and P' with the unknown value (a', b') are the *midpoints of the three boundary cords* of the balance region Ω. We put $c_\pm = c(a_\pm, b_\pm)$ and $c' = c(a', b')$ for abbreviation, see (2.10). Then we use for $k = 0, 1, 2$ the straight line paths γ_k from Fig. 2. For the corresponding path integrals

$$\int_{\gamma_k} x a(t, x)\, dx - x b(t, x)\, dt \quad \text{and} \quad \int_{\gamma_k} x b(t, x)\, dx - x c(a(t, x), b(t, x))\, dt$$

with the unknown weak entropy solution $a(t, x)$, $b(t, x)$ the numerical discretizations $\tilde{I}_{k,a}$ and $\tilde{I}_{k,b}$, respectively, are given by

$$\begin{cases} \tilde{I}_{0,a} = \displaystyle\int_{\gamma_0} x a'\, dx - x b'\, dt = a' \int_{\bar{x}-\Delta x}^{\bar{x}+\Delta x} x\, dx = 4 a' \lambda \Delta t\, \bar{x}, \\[4mm] \tilde{I}_{0,b} = \displaystyle\int_{\gamma_0} x b'\, dx - x c'\, dt = b' \int_{\bar{x}-\Delta x}^{\bar{x}+\Delta x} x\, dx = 4 b' \lambda \Delta t\, \bar{x}. \end{cases} \tag{3.2}$$
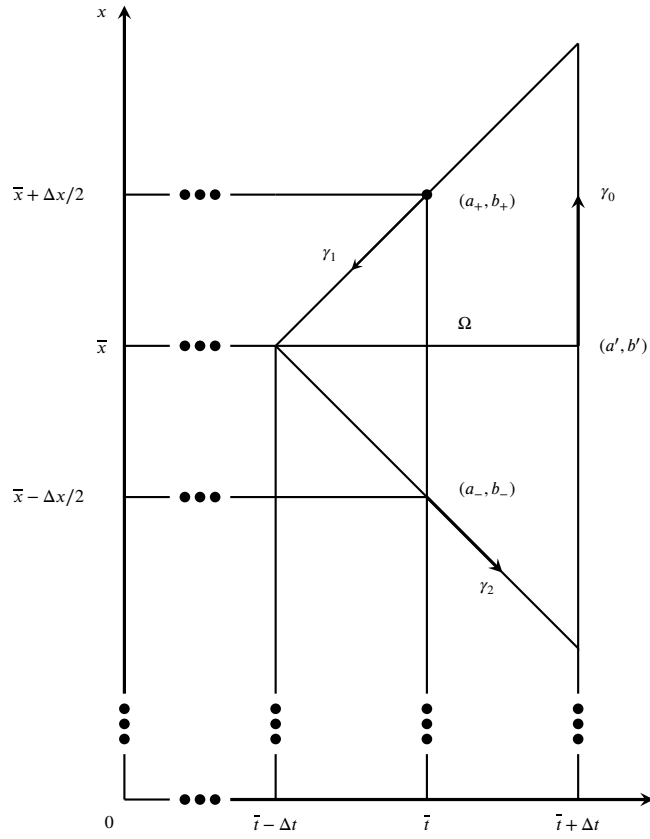
Fig. 2. The balance region Ω.

$$\begin{cases} \tilde{I}_{1,a} = \int\limits_{\gamma_1} xa_+\, dx - xb_+\, dt = -2(\lambda a_+ - b_+)\Delta t \left(\overline{x} + \frac{1}{2}\Delta x\right), \\[4mm] \tilde{I}_{1,b} = \int\limits_{\gamma_1} xb_+\, dx - xc_+\, dt = -2(\lambda b_+ - c_+)\Delta t \left(\overline{x} + \frac{1}{2}\Delta x\right). \end{cases} \tag{3.3}$$

$$\begin{cases} \tilde{I}_{2,a} = \int\limits_{\gamma_2} xa_-\, dx - xb_-\, dt = -2(\lambda a_- + b_-)\Delta t \left(\overline{x} - \frac{1}{2}\Delta x\right), \\[4mm] \tilde{I}_{2,b} = \int\limits_{\gamma_2} xb_-\, dx - xc_-\, dt = -2(\lambda b_- + c_-)\Delta t \left(\overline{x} - \frac{1}{2}\Delta x\right). \end{cases} \tag{3.4}$$

We recall that $\overline{x} \geq 0$ and distinguish two cases.

Case 1: First we assume that $\overline{x} > 0$. In this case we put

$$\tilde{q} = \frac{\Delta x}{2\overline{x}} \leq 1. \tag{3.5}$$

The numerical discretization of the first balance law in (2.11) gives

$$\tilde{I}_{0,a} = -\tilde{I}_{1,a} - \tilde{I}_{2,a}. \tag{3.6}$$

We obtain from (3.2), (3.3), (3.4), (3.5) and (3.6) for a' the explicit solution

$$a' = \frac{1}{2}\left(a_- + \frac{b_-}{\lambda}\right)(1 - \tilde{q}) + \frac{1}{2}\left(a_+ - \frac{b_+}{\lambda}\right)(1 + \tilde{q}). \tag{3.7}$$

For the numerical discretization of the second balance law in (2.11) we approximate the integral

$$\frac{1}{2}\iint\limits_{\Omega} (a - c)\, dt\, dx \quad \text{by} \quad \frac{1}{2}(a' - c')\iint\limits_{\Omega} dt\, dx = (a' - c')\Delta t\Delta x.$$

Now (3.2), (3.3), (3.4) give the following ansatz for the calculation of b':

$$\tilde{I}_{0,b} = -\tilde{I}_{1,b} - \tilde{I}_{2,b} + (a' - c')\Delta t \Delta x,$$

$$\Leftrightarrow \quad b' = \frac{1}{2}\left(b_+ - \frac{c_+}{\lambda}\right)(1 + \tilde{q}) + \frac{1}{2}\left(b_- + \frac{c_-}{\lambda}\right)(1 - \tilde{q}) + (a' - c')\frac{\tilde{q}}{2\lambda}. \tag{3.8}$$

Recall that $c = c(a,b)$ is given by (2.10) and thus the values $c_\pm$ are known. We further use (2.10) to substitute c' and obtain

$$b' - \frac{\tilde{q}}{3\lambda}\sqrt{4a'^2 - 3b'^2} = \frac{1}{2}\left(b_+ - \frac{c_+}{\lambda}\right)(1 + \tilde{q}) + \frac{1}{2}\left(b_- + \frac{c_-}{\lambda}\right)(1 - \tilde{q}) - a'\frac{\tilde{q}}{3\lambda}.$$

This is an implicit equation for b' where the right-hand side is known. Introducing the abbreviations

$$\eta = \frac{\tilde{q}}{3\lambda} \text{ and } \xi = \frac{1}{2}\left(b_- + \frac{c_-}{\lambda}\right)(1 - \tilde{q}) + \frac{1}{2}\left(b_+ - \frac{c_+}{\lambda}\right)(1 + \tilde{q}) - a'\eta \tag{3.9}$$

we obtain the implicit equation

$$b' = \xi + \eta\sqrt{4a'^2 - 3b'^2}. \tag{3.10}$$

This leads to a quadratic equation for b'. Lemma 3.1 gives

$$-a'(1 + \eta) < \xi < a'(1 - \eta)$$

for the quantity a' in (3.7). In order to apply Lemma 3.2 with a' instead of a we have to choose the solution

$$b' = \frac{\xi + \eta\sqrt{4a'^2(1 + 3\eta^2) - 3\xi^2}}{1 + 3\eta^2} \tag{3.11}$$

of (3.10) with the positive square root. Now b' is well defined with $|b'| < a'$, see the transformation (2.8) in state space.

Case 2: We assume that $\overline{x} = 0$. In this case we put

$$a' = a_+ - b_+/\lambda, \quad b' = 0. \tag{3.12}$$

Here we apply the reflection method from [14, Remark 4.5, equation (4.12)]. We note that $|b_+| < a_+$ implies $a' > 0$ and hence $|b'| = 0 < a'$ also in case 2. We summarize our results in the following

Theorem 3.3 (*Numerical solution (a', b') for the balance region Ω*). *Given are real quantities $\overline{x} \geq 0$ and $a_\pm$, $b_\pm$. Assume that $|b_\pm| < a_\pm$. We recall $\lambda \geq 1$ defined in terms of Δt and Δx and put $c_\pm = c(a_\pm, b_\pm)$ in (2.10).*

  (i) *For $\overline{x} > 0$ we calculate a' and b' from (3.5), (3.7), (3.9) and (3.11).*
  (ii) *For $\overline{x} = 0$ we calculate a' and b' from (3.12).*

Then we have $|b'| < a'$ in both cases. $\quad\square$

Definition 3.4 (*The function Euler*). *The state (a', b') from Theorem 3.3 defines the function Euler in (3.1).* $\quad\square$

Now we are able to formulate the numerical scheme for the solution of the initial-boundary value problem (2.12), (2.11). We construct staggered grid points in the computational domain D and compute the numerical solution at these grid points. Using the function Euler we obtain the evolution of the numerical solution in time, i.e., it allows us to construct the solution at time $t = t_{n+1}$ from the solution which is already calculated in the grid points at the former time step $t = t_n$.

  (I) The staggered grid points are $(t_n, x_{n,j}) \in D$ for $t_n = (n-1)\Delta t$, $n = 1, \ldots, 2N + 1$ and $j = 1, \ldots, M + N - \lfloor(n-1)/2\rfloor$ with

$$x_{n,j} = \begin{cases} (x_j + x_{j+1})/2 & \text{if } n \text{ is odd} \\ x_j & \text{if } n \text{ is even.} \end{cases}$$

  We want to calculate the numerical solution $(a_{n,j}, b_{n,j})$ at $(t_n, x_{n,j})$.
  (II) For $j = 1, \ldots, M + N$ we calculate the numerical solution $(a_{1,j}, b_{1,j})$ at the grid point $(t_1, x_{1,j}) = (0, (x_j + x_{j+1})/2)$ from the given initial data by

$$a_{1,j} = a_0\left(x_{1,j}\right), \quad b_{1,j} = b_0\left(x_{1,j}\right).$$

  This corresponds to taking the integral average of the initial data on (x_j, x_{j+1}) and using the midpoint rule as quadrature.
  (III) Assume that for a fixed *odd index* $n \in \{1, \ldots, 2N\}$ we have already determined the numerical solution $(a_{n,j}, b_{n,j})$ at the grid points $(t_n, x_{n,j})$, $j = 1, \ldots, M + N - (n-1)/2$.
  First we determine the solution $(a_{n+1,1}, b_{n+1,1})$ at the boundary point $(t_{n+1}, x_{n+1,1}) = (t_{n+1}, 0)$ according to (3.12). For this purpose we put $a_+ = a_{n,1}$, $b_+ = b_{n,1}$, $a_- = a_{n,1}$, $b_- = -b_{n,1}$ and have

$$(a_{n+1,1}, b_{n+1,1}) = \text{Euler}(a_-, b_-, a_+, b_+, 0, \Delta x, \lambda) \text{ with } b_{n+1,1} = 0.$$

Next we put $a_- = a_{n,j-1}$, $b_- = b_{n,j-1}$ and $a_+ = a_{n,j}$, $b_+ = b_{n,j}$ for $j = 2, \ldots, M + N - (n-1)/2$ and determine the values $a_{n+1,j}$, $b_{n+1,j}$ at time t_{n+1} and position $\overline{x} = x_{n+1,j} = x_j$ from

$$(a_{n+1,j}, b_{n+1,j}) = \text{Euler}(a_-, b_-, a_+, b_+, \overline{x}, \Delta x, \lambda).$$

(IV) Assume that for a fixed *even index* $n \in \{1, \ldots, 2N\}$ we have already determined the numerical solution $(a_{n,j}, b_{n,j})$ at the grid points $(t_n, x_{n,j})$, $j = 1, \ldots, M + N - n/2 + 1$.

We put $a_- = a_{n,j}$, $b_- = b_{n,j}$ and $a_+ = a_{n,j+1}$, $b_+ = b_{n,j+1}$ for $j = 1, \ldots, M + N - n/2$ and determine the values $a_{n+1,j}$, $b_{n+1,j}$ at time t_{n+1} and position $\overline{x} = x_{n+1,j} = (x_j + x_{j+1})/2$ from

$$(a_{n+1,j}, b_{n+1,j}) = \text{Euler}(a_-, b_-, a_+, b_+, \overline{x}, \Delta x, \lambda).$$

Based on Lemma 3.1 and 3.2 we obtain Theorem 3.3. Using (2.12) we can state the following

Theorem 3.5. *The numerical scheme described above preserves a positive pressure $p > 0$, provided the pressure is positive in the given initial data.* $\square$

4. Numerical results

We perform extensive numerical computations where we first validate the one-dimensional radially symmetric scheme (RadSymS) presented in Sect. 3 by means of self-similar solutions. Then we verify that the one-dimensional scheme can be used for the validation of genuinely multi-dimensional solvers. For this purpose we briefly summarize the numerical methods and models in Sect. 4.1. Then we set up different configurations for which we perform the computations in Sect. 4.2.

Finally, we compare the numerical results in Sect. 4.3.

4.1. Numerical methods

One-dimensional radially symmetric solver RadSymS. As described in Sect. 1 a radially symmetric solution of the ultra-relativistic Euler equations satisfies the quasi one-dimensional problem

$$
\begin{cases}
\dfrac{\partial}{\partial t}\left(x^{d-1}a\right) + \dfrac{\partial}{\partial x}\left(x^{d-1}b\right) = 0, \\[2mm]
\dfrac{\partial}{\partial t}\left(x^{d-1}b\right) + \dfrac{\partial}{\partial x}\left(x^{d-1}c\right) = \dfrac{d-1}{2}x^{d-2}(a-c), \\[2mm]
\lim_{t \searrow 0} a(t,x) = a_0(x), \quad \lim_{t \searrow 0} b(t,x) = b_0(x),
\end{cases}
\tag{4.1}
$$

for $t > 0$ and $x > 0$ representing the radial direction. Here $d = 2$ or $d = 3$ denotes the space dimension and $c = c(a, b)$ is given by (2.10). We are looking for weak solutions $a = a(t,x)$, $b = b(t,x)$ with $|b| < a$. For $d = 2$ the weak formulation of the system (4.1) is given in (2.11), and for $d = 3$ in [14, Equation (2.13)]. Using the transformation (2.8), its inverse (2.9) and the velocity

$$v = \frac{u}{\sqrt{1+u^2}} \quad \text{with } |v| < 1 \tag{4.2}$$

we replace the state variables a and b by p and v, respectively. We prescribe the initial pressure $p_0 = p(0, \cdot)$ as well as the initial velocity $v_0 = v(0, \cdot)$. Here we have chosen the variable v because the restriction $|v| < 1$ leads to better color plots (the variable u is unbounded).

The quasi one-dimensional problem (4.1) is approximately solved by the one-dimensional radially symmetric scheme presented in Sect. 3 with $N = 5000$. Note that for constant pressure $p_0 > 0$ and $v_0 = 0$, we obtain a stationary solution. This solution is exactly reconstructed by the one-dimensional radially symmetric scheme in Section 3. Such a steady part is contained in the solutions to the examples presented below.

Description of the multi-dimensional DG solver MultiWave. We also compare the results with the numerical solution of the original multi-dimensional initial value problem for the ultra-relativistic Euler equations (2.1), (2.2). For $j = 1, \ldots, d$ it reads

$$
\begin{cases}
\dfrac{\partial}{\partial t}\left(3\tilde{p} + 4\tilde{p}|\mathbf{u}|^2\right) + \displaystyle\sum_{k=1}^{d} \dfrac{\partial}{\partial x_k}\left(4\tilde{p}u_k\sqrt{1+|\mathbf{u}|^2}\right) = 0, \\[3mm]
\dfrac{\partial}{\partial t}\left(4\tilde{p}u_j\sqrt{1+|\mathbf{u}|^2}\right) + \displaystyle\sum_{k=1}^{d} \dfrac{\partial}{\partial x_k}\left(\tilde{p}\delta_{jk} + 4\tilde{p}u_j u_k\right) = 0, \\[3mm]
\tilde{p}(0,\mathbf{x}) = \tilde{p}_0(|\mathbf{x}|), \quad \mathbf{u}(0,\mathbf{x}) = \mathbf{u}_0(\mathbf{x}) = u_0(|\mathbf{x}|)\dfrac{\mathbf{x}}{|\mathbf{x}|}.
\end{cases}
\tag{4.3}
$$

Table 1
Discretization parameters for MultiWave.

	Ex. 1	Ex. 2	Ex. 3	Ex. 4	Ex. 5
Ω	$[-2,2]^2$	$[-2,2]^2$	$[-6,6]^2$	$[-6,6]^2$	$[-5,5]^2$
L	8	8	9	9	8
$\Delta\mathbf{x}_0$	$(2,2)$	$(2,2)$	$(4,4)$	$(4,4)$	$(2,2)$

We require radially symmetric solutions of this system, i.e., for $t \geq 0$ and $x = |\mathbf{x}| > 0$ the restrictions for pressure and velocity are given by

$$\tilde{p}(t,\mathbf{x}) = p(t,x), \quad \mathbf{u}(t,\mathbf{x}) = \frac{v(t,x)}{\sqrt{1-v(t,x)^2}} \cdot \frac{\mathbf{x}}{x}. \tag{4.4}$$

For $t = 0$ we obtain given initial data $\tilde{p}(0,\mathbf{x}) = p(0,x) = p_0(x)$ and

$$\mathbf{u}(0,\mathbf{x}) = \mathbf{u}_0(x) = \frac{v_0(x)}{\sqrt{1-v_0(x)^2}} \cdot \frac{\mathbf{x}}{x}, \tag{4.5}$$

and for $\mathbf{x} = \mathbf{0} \in \mathbb{R}^d$ we may also put $\mathbf{u}(0,\mathbf{0}) = \mathbf{0}$ and $v_0(0) = 0$.

The ultra-relativistic Euler equations are solved using a classical Runge-Kutta discontinuous Galerkin (RK-DG) method [4]. For this purpose we apply a modal DG scheme for the approximation of (4.3), which can be casted in the form of (B.1), and introduce the DG space

$$S_h^p := \{f \in L^2(\Omega) : \ f|_{V_\lambda} \in \Pi_{p-1}(V_\lambda) \ \forall \ \lambda \in \mathcal{I}\}. \tag{4.6}$$

Here $\Pi_{p-1}(V)$ denotes the space of polynomials on the element V of maximal degree with respect to l_∞ less than p, i.e., $\dim(\Pi_{p-1}(V)) = p^d$. For the finite-dimensional space S_h^p we introduce a basis $\Phi := \{\phi_{\lambda,i}\}_{\lambda \in \mathcal{I}, i=1,\dots,p^d}$, i.e., $S_h^p = \text{span}\,\Phi$ of orthogonal and compactly supported basis functions $\phi_{\lambda,i}$. The solution of (B.1) is approximated by a piecewise polynomial in the DG space S_h^p, i.e.,

$$w_h(t,\cdot) = \sum_{\lambda \in \mathcal{I}} \sum_{i=1,\dots,p^d} v_{\lambda,i}(t)\phi_{\lambda,i}(\cdot) \in S_h^p. \tag{4.7}$$

By a standard procedure employing the orthogonality property and the local support of the basis functions, see [4], we obtain the system of ordinary differential equations in time for the coefficients $v_{\lambda,i}$:

$$\frac{\partial v_{\lambda,i}}{\partial t} = \int_{V_\lambda} \mathbf{f}(w_h) \cdot \nabla \phi_{\lambda,i}\,d\mathbf{x} - \int_{\partial V_\lambda} \hat{\mathbf{f}}(w_h^+, w_h^-, \vec{n}_\lambda)\phi_{\lambda,i}\,d\Gamma. \tag{4.8}$$

Here w_h^+ denotes the inner and w_h^- the outer value of w_h at the boundary of V_λ. Furthermore $\vec{n}_\lambda$ is the outward pointing unit normal vector corresponding to V_λ. The integrals are approximated by Gauss quadrature formulae of order p and at the cell interfaces we use a numerical flux $\hat{f}$. Finally, to obtain a fully-discrete method, we have to discretize the system in time. In particular, for the present work we apply a third order DG scheme using piecewise polynomial elements of order $p = 3$ and a third-order explicit SSP-Runge-Kutta method with three stages for the time discretization. For a numerical flux we choose the local Lax-Friedrichs flux. The Gibbs phenomena near to discontinuities are suppressed by the minmod limiter from [4], where we employ the eigenvalues and corresponding left- and right-eigenvectors of the flux Jacobian. Details can be found in the Appendix B.

Because of the explicit time discretization we restrict the timestep size by means of a CFL number. The efficiency of the scheme is improved by local grid adaption where we employ the multiresolution concept based on multiwavelets. The key idea is to perform a multiresolution analysis on a sequence of nested grids providing a decomposition of the data on a coarse scale and a sequence of details that encode the difference of approximations on subsequent resolution levels. The detail coefficients become small when the underlying data are locally smooth and, hence, can be discarded when dropping below a threshold value ε_{thresh}. By means of the thresholded sequence a new, locally refined grid is determined. Details on this concept can be found in [11,8–10].

For all examples, we set the CFL number to $CFL = 0.06$. Table 1 summarizes the computational domain $\Omega \subset \mathbb{R}^2$, the maximum refinement level $L \in \mathbb{N}$ and the cell size $\Delta\mathbf{x}_0 \in \mathbb{R}^2$ at the coarsest refinement level for each example. Due to the dyadic grid hierarchy in MultiWave the cell size at refinement level l is $\Delta\mathbf{x}_l = 2^{-l}\Delta\mathbf{x}_0$, for $l = 0,\dots,L$.

4.2. Benchmark tests

In the following we set up several radially symmetric problems where two of them provide self-similar solutions, see Example 1 and 2. All of these configurations may serve as benchmark problems for the validation of multi-dimensional solvers, e.g., finite volume schemes or discontinuous Galerkin (DG) schemes.

Example 1: Solutions including a shock and a stationary part. Following [18] self-similar solutions can be constructed solving an ODE system in radial direction x. These solutions are in particular constant along rays $\xi = x/t$ or, equivalently, $\vartheta = t/x$. Such solutions are used for validation purposes for both the one-dimensional radially symmetric solver and the multi-dimensional DG solver.

Table 2
Example 1: Shock states for $d = 2, 3$.

	$\tilde{s}$	p_-	v_-	p_+	v_+
$d = 2$	0.45503	15.75505	0	5.71869	−0.41629
$d = 3$	0.52314	25.56463	0	17.16524	−0.17106

We consider constant initial data with pressure $p_0 = 1$ and radial velocity $v_0 \in (-1, 0)$. Due to [18, Section 2.3] there is a solution $p(t, x) = P(\vartheta)$ and $v(t, x) = V(\vartheta)$ depending only on $\vartheta = t/x$ for $t, x > 0$, with a single straight line shock emanating from the zero point. Let $\tilde{s} \in (0, 1)$ be the unknown constant shock speed. Then we put $v_- = 0$ and can find an unknown pressure $p_- > 0$ with

$$p(t, x) = p_-, \quad v(t, x) = v_- = 0 \quad \text{for } x < \tilde{s} \cdot t.$$

Due to the Rankine-Hugoniot shock conditions introduced in [13, Section 4.4] we obtain from [13, page 82] for a so called 3-shock after a lengthy calculation the algebraic shock conditions

$$\frac{p_+}{p_-} = \frac{9\tilde{s}^2 - 1}{3(1 - \tilde{s}^2)}, \quad v_+ = \frac{3}{2}\tilde{s} - \frac{1}{2\tilde{s}}, \quad v_- = 0, \tag{4.9}$$

$$0 < p_+ < p_-, \quad \frac{1}{3} < \tilde{s} < \frac{1}{\sqrt{3}}.$$

Here p_-, v_- are the values of pressure and velocity left to the 3-shock, and p_+, v_+ are the values of pressure and velocity right to the 3-shock. Due to Lai [18, Section 2.3] the solution $p = P(\vartheta)$, $v = V(\vartheta)$ satisfies the initial value problem of ordinary differential equations

$$\dot{V}(\vartheta) = (d - 1)\frac{V(V - \vartheta)(1 - V^2)}{3(\vartheta V - 1)^2 - (V - \vartheta)^2}, \quad V(0) = v_0 \in (-1, 0),$$

$$\dot{P}(\vartheta) = (d - 1)\frac{4PV(\vartheta V - 1)}{3(\vartheta V - 1)^2 - (V - \vartheta)^2}, \quad P(0) = p_0 = 1. \tag{4.10}$$

Moreover, we show in Appendix A that Lai's results guarantee a unique solution for $0 \le \vartheta < \vartheta_{max}$ with a certain value $\vartheta_{max} > \sqrt{3}$ and a unique value $\tilde{\vartheta} \in (\sqrt{3}, \min(3, \vartheta_{max}))$ such that

$$V(\tilde{\vartheta}) = \frac{3}{2\tilde{\vartheta}} - \frac{\tilde{\vartheta}}{2}. \tag{4.11}$$

After having determined $\tilde{\vartheta}$ we finally obtain

$$\tilde{s} = \frac{1}{\tilde{\vartheta}}, \quad v_+ = V(\tilde{\vartheta}), \quad p_+ = P(\tilde{\vartheta}), \quad p_- = p_+ \frac{3(1 - \tilde{s}^2)}{9\tilde{s}^2 - 1}. \tag{4.12}$$

For our numerical simulation we choose $d = 2$, a constant initial pressure $p_0 = 1$ and a constant initial velocity $v_0 = -1/\sqrt{2}$. This corresponds to the following initial data for the original initial value problem (4.3)

$$\tilde{p}(0, \mathbf{x}) = 1 \quad \text{and} \quad \mathbf{u}(0, \mathbf{x}) = -\frac{\mathbf{x}}{|\mathbf{x}|}, \quad \mathbf{x} \in \mathbb{R}^d \setminus \{\mathbf{0}\}.$$

The radially symmetric solution of (4.3) is determined by the solution of the ODE system (4.10) which gives a shock wave moving at constant speed $\tilde{s}$. We want to point out that these ODEs are written in terms of $\vartheta = t/x$. Thus the initial data $P(0)$ and $V(0)$ for (4.10) prescribe the solution for (4.3) at infinity given by $p_0 = P(0)$ and $v_0 = V(0)$. The ODE system (4.10) is solved by applying the classical fourth order RK-scheme with step size $h = 10^{-6}$. For the computation of $\tilde{\vartheta}$ the ODE solver is run until (4.11) is satisfied with a tolerance of $\varepsilon = 10^{-9}$. The solution values for the shock speed, the states ahead and behind of the shock, respectively, are presented in Table 2. Here the numerical values for $\tilde{s}$ and for p_-, v_- on the plateau are the same up to three digits after the decimal point. We want to mention that for $d = 3$ the values given in (4.11) and (4.12) show a good agreement with the numerical results given in [14, Section 5, Example 3].

Example 2: Self-Similar Expansion. In this example we prescribe initial data leading to a smooth self-similar solution by applying Lai's approach as in Example 1. Note that for $d = 3$ the solution will expand into vacuum at the speed of light when the initial value for v_0 is close enough to one. We do not consider this case here and refer to [18] for more details. For our numerical simulation we choose $d = 2$, a constant initial pressure $p_0 = 1$ and a constant initial velocity $v_0 = 1/\sqrt{2}$. This corresponds to the following initial data for the original initial value problem (4.3)

$$\tilde{p}(0, \mathbf{x}) = 1 \quad \text{and} \quad \mathbf{u}(0, \mathbf{x}) = \frac{\mathbf{x}}{|\mathbf{x}|}, \quad \mathbf{x} \in \mathbb{R}^d \setminus \{\mathbf{0}\}.$$

The solution consists of a rarefaction wave that is determined by the ODE (4.10). In contrast to Example 1 there is no shock.

Example 3: Expansion of a Spherical Bubble. Next we consider the expansion of a spherical bubble in $d = 2$ with the following initial data

$$p_0(x) = \begin{cases} 1 & \text{for } 0 \le x \le 1 \\ 0.1 & \text{for } x > 1, \end{cases} \qquad v_0(x) = 0.$$

These initial values correspond to the following initial values for the original initial value problem (4.3)

$$\tilde{p}(0, \mathbf{x}) = \begin{cases} 1 & \text{for } 0 \le |\mathbf{x}| \le 1 \\ 0.1 & \text{for } |\mathbf{x}| > 1, \end{cases} \qquad \mathbf{u}(0, \mathbf{x}) = \mathbf{0}.$$

Example 4: Collapse of a Spherical Bubble. Next we study the collapse of a spherical bubble in $d = 2$ with the following initial data

$$p_0(x) = \begin{cases} 0.1 & \text{for } 0 \le x \le 1 \\ 1 & \text{for } x > 1, \end{cases} \qquad v_0(x) = 0.$$

These initial values correspond to the following initial values for the original initial value problem (4.3)

$$\tilde{p}(0, \mathbf{x}) = \begin{cases} 0.1 & \text{for } 0 \le |\mathbf{x}| \le 1 \\ 1 & \text{for } |\mathbf{x}| > 1, \end{cases} \qquad \mathbf{u}(0, \mathbf{x}) = \mathbf{0}.$$

Example 5: Initially Sine–Shaped Radial Velocity. Finally, we study initial data with a velocity in radial direction described by a sine function, i.e.,

$$p_0(x) = 1, \quad u_0(x) = \begin{cases} \sin(2\pi x), & x < 1, \\ 0, & x \ge 1. \end{cases}$$

These correspond to the following initial data for the multi-dimensional simulation

$$\tilde{p}(0, \mathbf{x}) = 1, \quad \mathbf{u}(0, \mathbf{x}) = \begin{cases} \sin(2\pi |\mathbf{x}|) \dfrac{\mathbf{x}}{|\mathbf{x}|}, & |\mathbf{x}| < 1, \\ 0, & \mathbf{x} \ge 1. \end{cases}$$

4.3. Discussion of results

For all examples we perform computations with the one-dimensional radially symmetric scheme RadSymS and the multi-dimensional DG solver MultiWave for comparisons. Details on the discretization parameters can be found in Sect. 4.1. In Figs. 3 – 7 for Examples 1 – 5, respectively, we present 2D-results in the t–x plane and a line plot of the solution in radial direction at the final time t_{end}. We compare the results of the two solvers by means of the pressure p and the velocity v. Additionally, for Examples 1 and 2 we compare the solutions also with the reference solution that can be determined for self-similar problems by solving the ODE (4.10) in the smooth part and using the jump conditions (4.12) to determine the stationary part in Example 1, see Sect. 4.2.

Example 1 and 2. The results reported in Figs. 3 and 4 clearly show a good agreement of both numerical methods with the reference solution provided by an ODE solver for the final time $t_{end} = 1$ in radial direction. Due to the self-similar structure of the solution we omit the presentation of results in the t–x plane.

Example 3. Initially, the pressure inside the bubble is ten times larger than outside, which leads to a fast expansion of the bubble into the outer low pressure area. This in turn gives rise to the formation of another low pressure area. We observe the formation of a shock wave, running towards the new low pressure area and reaching the zero point around time $t = 5.032$. The formation of this new shock wave is a peculiar nonlinear phenomenon. Shortly before the shock reaches the zero point the pressure takes very low values, but its reflection from the zero point depicted in Fig. 5 (a) and (b) indicates a blow up of the pressure in a very small time-space range near the boundary. This is similar to [14, Section 5, Example 4], but here the blow up is weaker than in three space dimensions, and its illustration requires a higher numerical resolution. This may be the reason why this phenomenon was neglected up to day for the explosion test problem with an initial bubble. We expect a similar behavior for the corresponding solution of the explosion problem with the classical Euler equations.

From the depicted solution at time $t = 6$ we observe the reflected shock curve at radius around $x = 0.55$. The results in the t–x plane given in Fig. 5 (a) and (b) show the expansion of the bubble and the formation of the new shock which focuses at the origin and then is reflected again. At the focus point the pressure rises drastically in a small vicinity of the origin and away from that the pressure values do not vary a lot. Therefore we present a zoom plot of the pressure. We observe an excellent agreement of both numerical methods for the velocity in Fig. 5 (b). For the pressure the results also agree well, except close to the reflection point of the shock at the origin where the DG method cannot resolve this structure due to the resolution of the multi-dimensional method, see Fig. 5 (a). Additionally, we compare both methods at final time $t_{end} = 6$ where the solutions coincide very well, see Fig. 5 (c) and (d).

Example 4. The results in the t–x plane, see Fig. 6 (a) and (b), show the collapse of the bubble with a focus point at the origin which then is reflected again. At the focus point the pressure rises drastically in a small vicinity of the origin and away from that the pressure values do not vary a lot. Thus, we again present a zoom plot of the pressure for this example. We observe an excellent
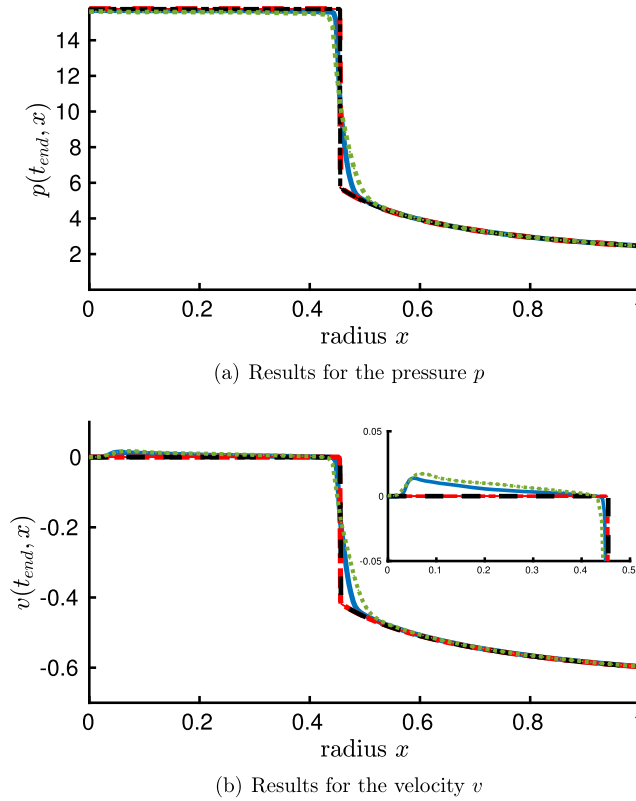
(a) Results for the pressure p

(b) Results for the velocity v

Fig. 3. Example 1: Comparison for MultiWave (green $L = 8$, blue $L = 9$) and RadSymS (red) in radial direction with the solution of ODE system (4.10) (black) at final time $t_{end} = 1$ for the pressure p, see (a), and velocity v, see (b). (For interpretation of the colors in the figure(s), the reader is referred to the web version of this article.)

agreement of both numerical methods for the velocity in Fig. 6 (b). For the pressure the results also agree well except close to the reflection point of the shock at the origin where the DG method cannot resolve this structure due to the resolution of the multi-dimensional method, see Fig. 6 (a). Additionally, we compare both methods at time $t_{end} = 6$ where the solutions coincide very well, see Fig. 6 (c) and (d).

    Example 5. The results in the t–x plane, see Fig. 7 (a) and (b), show a complex wave structure for the velocity and a high pressure focus at around time $t = 0.77$. Again, we present a zoom plot of the pressure for this example. We observe an excellent agreement of both numerical methods for the velocity in Fig. 7 (b). For the pressure the results also agree well, except close to the reflection point of the shock at the origin where the DG method cannot resolve this structure due to the resolution of the multi-dimensional method, see Fig. 7 (a). Additionally, we compare both methods at final time $t_{end} = 6$ where the solutions coincide very well, see Fig. 7 (a) and (b).

    For all simulations with the multi-dimensional DG solver MultiWave we note some perturbations near the focus point after wave reflection in this point. These can be observed in the one-dimensional plots for the velocity at the final time t_{end}, see in particular Fig. 3 (b) and 7 (d). Most likely, the perturbations are caused by a dimensional effect introduced by the Cartesian grids that are not able to preserve and resolve radial symmetry. This dimensional effect can be clearly observed in the adaptive grids not presented here. Under grid refinement the perturbations become smaller and are located more closely to the focus point. Exemplarily, we perform two computations with the DG solver with maximal refinement level $L = 8$ and $L = 9$ for Example 1. In Fig. 3 (a) and (b) we observe that the perturbation becomes smaller with higher resolution.

5. Conclusion

    In the present work we studied radially symmetric solutions for the ultra-relativistic Euler equations in two and three space dimensions. An efficient numerical scheme for the computation of such one-dimensional radially symmetric solutions was developed.

    Furthermore, we computed solutions for different sets of initial data exhibiting complex wave structures. In the case of self-similar solutions we compared our method with a reference solution obtained by solving simplified ODEs along a ray $\vartheta = t/x = const$ for fixed time t_{end}. These comparisons show an excellent agreement of the proposed one-dimensional radially symmetric method with the reference solution at some fixed time t.

    By construction one-dimensional solver is capable of calculating radially symmetric solutions very efficiently in comparison to multi-dimensional solvers and, thus, provides reference solutions in the t–x plane for comparison with multi-dimensional solutions.

(a) Results for the pressure p
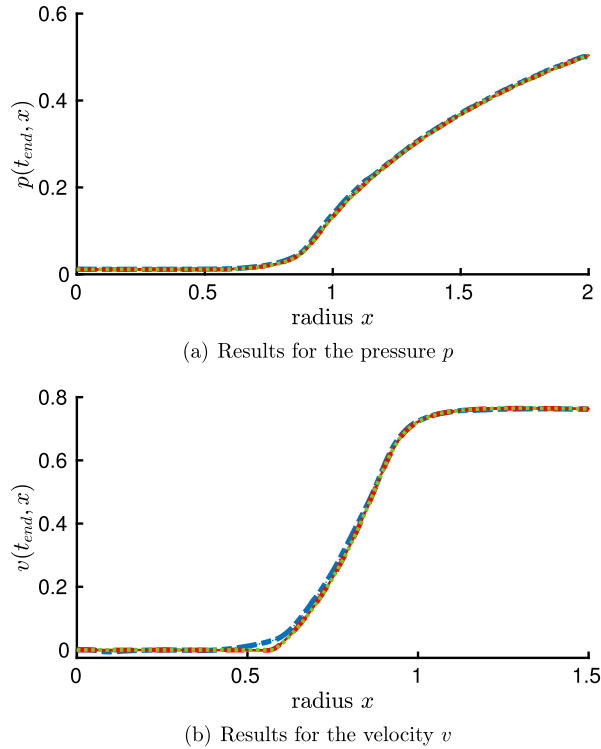

(b) Results for the velocity v

Fig. 4. Example 2: Comparison for MultiWave (blue) and RadSymS (red) in radial direction with the solution of ODE system (4.10) (green) at final time $t_{end} = 1$ for the pressure p, see (a), and velocity v, see (b).

Exemplarily, this was demonstrated by performing simulations for the two-dimensional initial value problem applying the DG-solver MultiWave. These solutions were compared with solutions of the one-dimensional radially symmetric solver. The solutions showed a very good agreement. For this a high resolution was needed for the multi-dimensional DG solver resulting in high computational cost.

Finally, we want to emphasize that the examples considered here are very much suited as challenging genuinely multi-dimensional benchmark problems for numerical methods designed for hyperbolic PDEs. The one-dimensional radially symmetric solver can provide non-trivial reference solutions at low cost and high accuracy. These reference solutions may be used for validation of multi-dimensional solvers.

CRediT authorship contribution statement

Matthias Kunik: Writing – review & editing, Writing – original draft, Validation, Formal analysis, Conceptualization. **Adrian Kolb:** Writing – review & editing, Writing – original draft, Visualization, Validation, Software, Conceptualization. **Siegfried Müller:** Writing – review & editing, Writing – original draft, Validation, Software, Funding acquisition, Formal analysis. **Ferdinand Thein:** Writing – review & editing, Writing – original draft, Visualization, Validation, Funding acquisition, Formal analysis, Conceptualization.

Declaration of competing interest

The authors declare that they have no known competing financial interests or personal relationships that could have appeared to influence the work reported in this paper.

Data availability

Data will be made available on request.
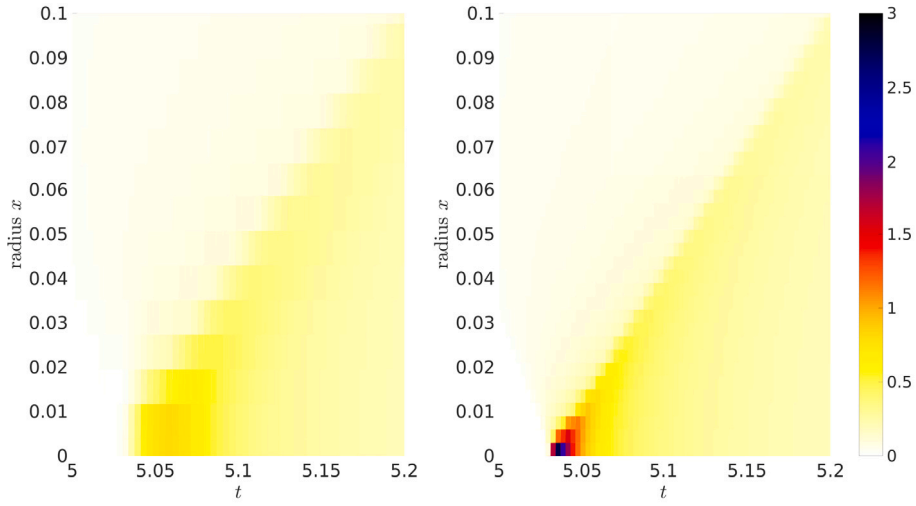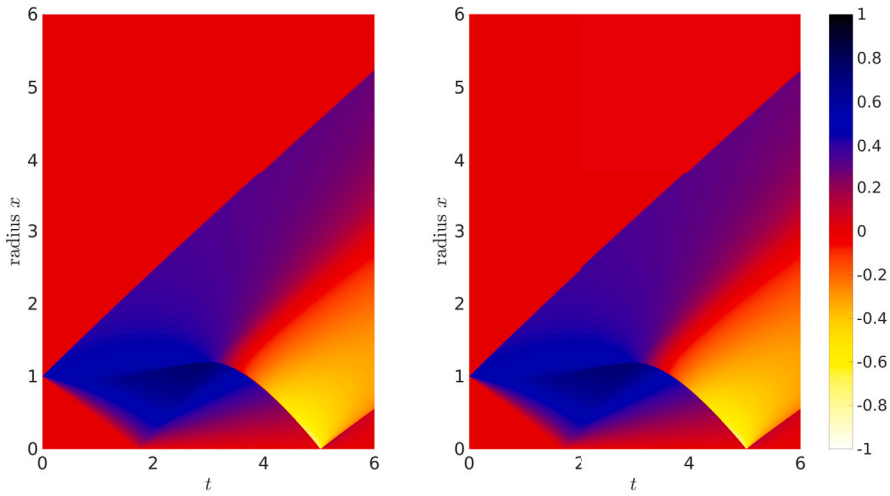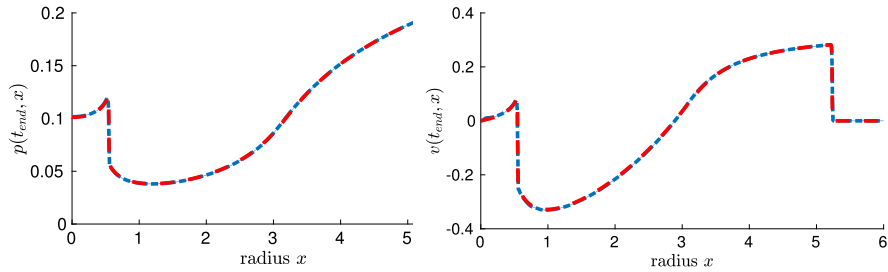
Acknowledgement

(a) Results for the pressure p

(b) Results for the velocity v

(c) Results for the pressure p

(d) Results for the velocity v

Fig. 5. Example 3: Comparison for MultiWave (left) and RadSymS (right) in the t–x plane, see (a), (b). Further RadSymS (red) and MultiWave (blue) are compared in radial direction at final time $t_{end} = 6$, see (c), (d), for pressure p and velocity v.
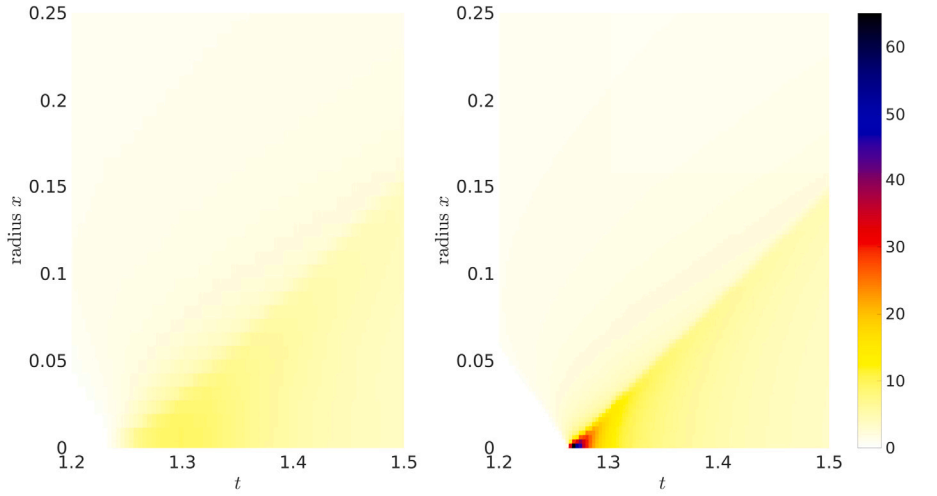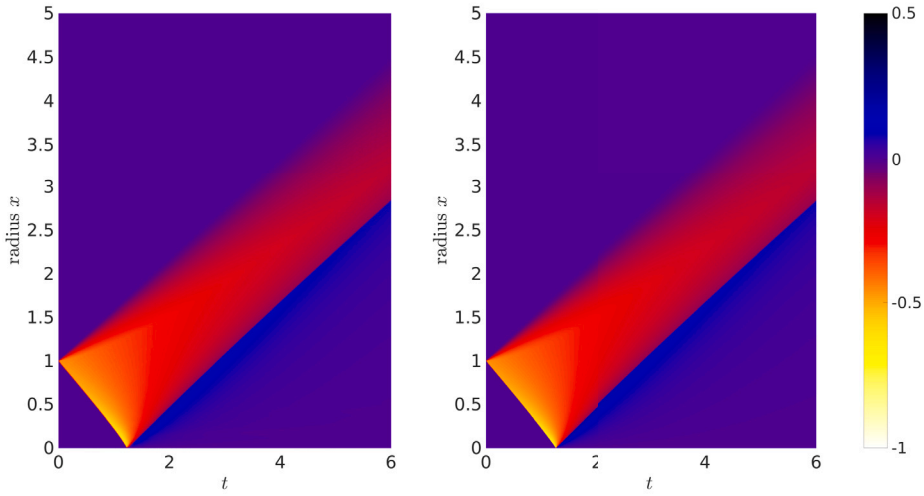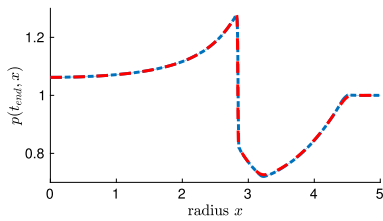
(a) Results for the pressure p

(b) Results for the velocity v

(c) Results for the pressure p

(d) Results for the velocity v

Fig. 6. Example 4: Comparison for MultiWave (left) and RadSymS (right) in the $t–x$ plane, see (a), (b). Further RadSymS (red) and MultiWave (blue) are compared in radial direction at final time $t_{end} = 6$, see (c), (d), for pressure p and velocity v.

Appendix A. Application of Geng Lai's analysis

It is shown by Geng Lai in [18, Section 2] that for special solutions depending only on $\vartheta = t/x > 0$ the system (2.1), (2.2) can be reduced to the system of ODEs (4.10). It is sufficient to discuss

$$\dot{V}(\vartheta) = (d - 1)\frac{V(V - \vartheta)(1 - V^2)}{f(\vartheta, V)} \quad \text{with} \tag{A.1}$$
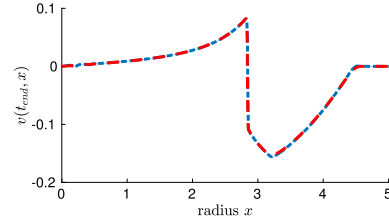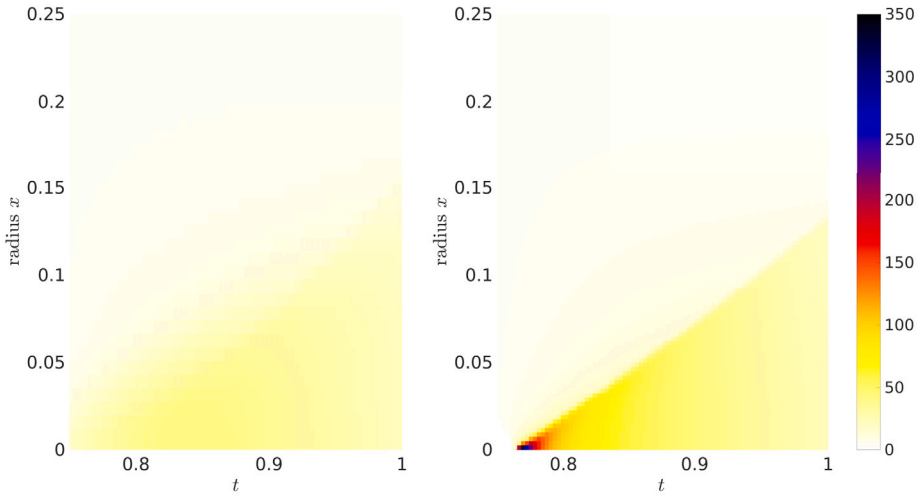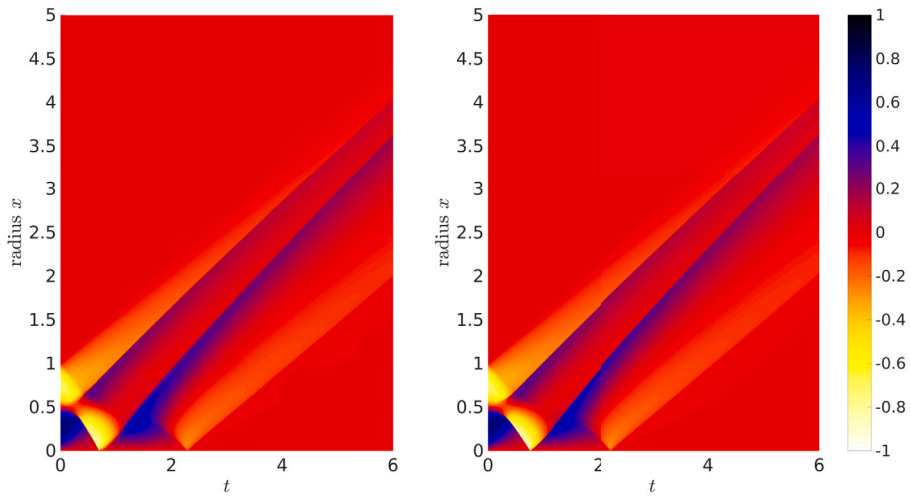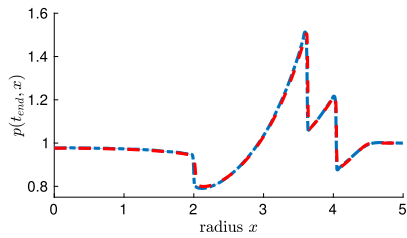
(a) Results for the pressure p

(b) Results for the velocity v

(c) Results for the pressure p
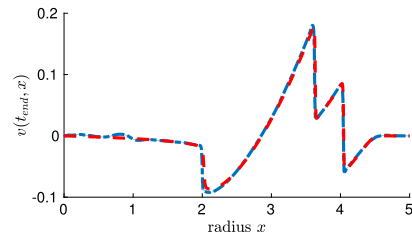
(d) Results for the velocity v

Fig. 7. Example 5: Comparison for MultiWave (left) and RadSymS (right) in the t–x plane, see (a), (b). Further RadSymS (red) and MultiWave (blue) are compared in radial direction at final time $t_{end} = 6$, see (c), (d), for pressure p and velocity v.

$$f(\vartheta, V) = 3(\vartheta V - 1)^2 - (V - \vartheta)^2$$

for $d = 2$ and $d = 3$ space dimensions, respectively. The differential equation (A.1) has to be supplemented by an initial condition $V(0) = v_0$ with $|v_0| < 1$. For $v_0 \in (0, 1)$ we obtain continuous solutions, see [18, Section 2.2] for further details. For our discussion we want to focus on the case $-1 < v_0 < 0$ where shock wave solutions occur. Hence we require an initial condition

$$V(0) = v_0 \in (-1, 0). \tag{A.2}$$

By $(0, \vartheta_{max})$ with $\vartheta_{max} > 0$ we denote the maximal existence interval for the solution $V = V(\vartheta)$ of the initial value problem (A.1), (A.2). It is shown in [18, Section 2.3] that $V(\vartheta) < 0$ for $\vartheta \in [0, \sqrt{3}]$ and $v_0 \in (-1, 0)$. Lai obtained that $\sqrt{3} < \vartheta_{max} < \infty$ for the initial condition (A.2). Note that we have the normalized speed of light $c = 1$. The values $V = \pm 1$ and $V = 0$ are fixed points for the ODE (A.1). Hence it is sufficient to study solutions $V = V(\vartheta) \in (-1, 0)$ with $\vartheta \in (0, \vartheta_{max})$. In order to show that (4.11) has a unique solution $\tilde{\vartheta} \in (\sqrt{3}, \min(3, \vartheta_{max}))$ we first determine the sign of the denominator $f(\vartheta, V)$ on the right-hand side of (A.1). Initially we have $f(0, v_0) = 3 - v_0^2 > 0$. As long as $-1 < V < 0$ we have $V < 0$, $V - \vartheta < 0$ and $1 - V^2 > 0$ for the three factors in the nominator of the right-hand side of (A.1). We conclude that $f(\vartheta, V) = 0$ can only occur at the singular point $\vartheta = \vartheta_{max}$ and obtain by the intermediate value theorem that $f(\vartheta, V(\vartheta)) > 0$ and $\dot{V}(\vartheta) > 0$ for $0 < \vartheta < \vartheta_{max}$. Hence V is strictly monotonically increasing in $(0, \vartheta_{max})$. The equation $f(\vartheta, V) = 0$ can be solved explicitly. Reformulating the denominator gives

$$
\begin{aligned}
0 &= 3(\vartheta V - 1)^2 - (V - \vartheta)^2 \\
&= \left(\sqrt{3}(\vartheta V - 1) + (V - \vartheta) \right) \left(\sqrt{3}(\vartheta V - 1) - (V - \vartheta) \right).
\end{aligned}
\tag{A.3}
$$

We obtain two possible functions where the denominator vanishes, namely $\overline{V}_1, \overline{V}_2 : (\sqrt{3}, \infty) \mapsto \mathbb{R}$ with

$$
\overline{V}_1(\vartheta) = \frac{\vartheta + \sqrt{3}}{\sqrt{3}\vartheta + 1} > 0 \quad \text{and} \quad \overline{V}_2(\vartheta) = -\frac{\vartheta - \sqrt{3}}{\sqrt{3}\vartheta - 1} < 0.
\tag{A.4}
$$

Since $V < 0$, we can rule out the positive function $\overline{V}_1$. Due to Lai we obtain from the monotonicity of the solution V that

$$
\lim_{\vartheta \nearrow \vartheta_{max}} V(\vartheta) = \sup_{0 < \vartheta < \vartheta_{max}} V(\vartheta) = \overline{V}_2(\vartheta_{max}), \quad \lim_{\vartheta \nearrow \vartheta_{max}} \frac{dV}{d\vartheta} = +\infty.
\tag{A.5}
$$

A straightforward calculation shows for the function $\overline{V}_2$ in (A.4) that

$$
\overline{V}_2(\vartheta) > \frac{3}{2\vartheta} - \frac{\vartheta}{2}
\tag{A.6}
$$

for all $\vartheta > \sqrt{3}$. The right-hand side of (A.6) vanishes at $\vartheta = \sqrt{3}$ and takes the value -1 for $\vartheta = 3$. Using the intermediate value theorem we finally conclude from (A.6) and the first relation in (A.5) that (4.11) has a unique solution

$$
\tilde{\vartheta} \in (\sqrt{3}, \min(3, \vartheta_{max})).
\tag{A.7}
$$

This guarantees a solution with a shock, see Example 1 in Sect. 4.2. According to (4.12) this shock propagates with constant speed $\tilde{s} = 1/\tilde{\vartheta}$.

Estimation (A.7) contains the unknown quantity ϑ_{max}. Now we derive a better suited explicitly given upper bound for $\tilde{\vartheta}$. For this purpose we note that the bijective mapping $V_0 : [\sqrt{3}, 3] \mapsto [-1, 0]$ with

$$
V_0(\vartheta) = \frac{3}{2\vartheta} - \frac{\vartheta}{2}
\tag{A.8}
$$

has the inverse function $V_0^{-1} : [-1, 0] \mapsto [\sqrt{3}, 3]$ given by

$$
V_0^{-1}(v) = \sqrt{v^2 + 3} - v.
\tag{A.9}
$$

The solution V of the initial value problem is strictly monotonically increasing with $V(0) = v_0$, whereas V_0 is strictly monotonically decreasing for $\vartheta > \sqrt{3}$. Thus, we obtain again from $V_0^{-1}(0) = \sqrt{3}$ and $V_0^{-1}(-1) = 3$ the estimation

$$
\sqrt{3} < \tilde{\vartheta} < \sqrt{v_0^2 + 3} - v_0 < 3.
\tag{A.10}
$$

With (A.10) we have obtained useful bounds for $\tilde{\vartheta}$ and, hence, for the shock speed $\tilde{s}$ in (4.12) depending only on the initial data but independent of ϑ_{max}. Moreover, this result holds for $d = 2$ as well as for $d = 3$ space dimensions.

Appendix B. Eigensystem for ultra-relativistic Euler equations

The ultra-relativistic Euler equations can be written in conservative form

$$
\partial_t \boldsymbol{w} + \sum_{k=1}^{d} \partial_{x_k} \boldsymbol{f}_k(\boldsymbol{w}) = \boldsymbol{0}
\tag{B.1}
$$

for the vector of conserved variables $\boldsymbol{w} = (w_1, \ldots, w_d, w_{d+1}) = (\overline{\boldsymbol{w}}, w_{d+1}) \in \mathbb{R}^{d+1}$ with $d \in \{1, 2, 3\}$ consisting of momentum $\overline{\boldsymbol{w}} = (w_1, \ldots, w_d) \in \mathbb{R}^d$ and energy w_{d+1} and fluxes in the kth coordinate direction

$$
\boldsymbol{f}_k(\boldsymbol{w}) = p \boldsymbol{e}_k + \sum_{i=1}^{d} \frac{w_i w_k}{w_{d+1} + p} \boldsymbol{e}_i + w_k \boldsymbol{e}_{d+1}, \ k = 1, \ldots, d,
\tag{B.2}
$$

with e_i the ith unit vector in $\mathbb{R}^{d+1}$. This system is closed by an equation of state for the pressure

$$p = p(\boldsymbol{w}) \tag{B.3}$$

to be specified below. For its discretization classical finite volume schemes or DG schemes may be applied. For this purpose, numerical fluxes in normal direction $\overline{\boldsymbol{n}} \in \mathbb{R}^d$, $|\overline{\boldsymbol{n}}| = 1$, have to be computed at the interfaces of the elements typically requiring the eigenvalues and eigenvectors of the corresponding flux Jacobian. In the following we determine the eigensystem to the Jacobian of the flux in normal direction

$$\boldsymbol{f}_{\overline{\boldsymbol{n}}}(\boldsymbol{w}) := \sum_{k=1}^{d} \boldsymbol{f}_k(\boldsymbol{w}) n_k. \tag{B.4}$$

The flux Jacobian is determined by

$$\boldsymbol{A}_{\overline{\boldsymbol{n}}} := \partial_{\boldsymbol{w}} \boldsymbol{f}_{\overline{\boldsymbol{n}}}(\boldsymbol{w}) = \begin{pmatrix} \overline{\boldsymbol{A}} & \overline{\boldsymbol{a}} \\ \overline{\boldsymbol{n}}^T & 0 \end{pmatrix} \tag{B.5}$$

with

$$\overline{\boldsymbol{A}} = \overline{\boldsymbol{n}} \otimes \nabla_{\overline{\boldsymbol{w}}} p + \frac{w_n}{w_{d+1} + p} \overline{\boldsymbol{I}}_{d \times d} + \frac{1}{w_{d+1} + p} \overline{\boldsymbol{w}} \otimes \overline{\boldsymbol{n}} - \frac{w_n}{(w_{d+1} + p)^2} \overline{\boldsymbol{w}} \otimes \nabla_{\overline{\boldsymbol{w}}} p,$$

$$\overline{\boldsymbol{a}} = \partial_{w_{d+1}} p \, \overline{\boldsymbol{n}} - \frac{1 + \partial_{w_{d+1}} p}{(w_{d+1} + p)^2} w_n \overline{\boldsymbol{w}}.$$

To compute the eigenvalues we need to determine the characteristic polynomial of the matrix

$$\boldsymbol{B}_{\overline{\boldsymbol{n}}} := \boldsymbol{A}_{\overline{\boldsymbol{n}}} - \lambda \boldsymbol{I}_{(d+1) \times (d+1)}.$$

The derivation is elementary but tedious work performing some algebraic manipulations. It will be helpful to introduce an orthonormal system $\overline{\boldsymbol{t}}_i \in \mathbb{R}^d$, $i = 2, \dots, d$, to the normal $\overline{\boldsymbol{n}} \equiv \overline{\boldsymbol{t}}_1$ inducing the orthogonal matrix

$$\overline{\boldsymbol{T}}_{\overline{\boldsymbol{n}}} := (\overline{\boldsymbol{t}}_1 = \overline{\boldsymbol{n}}, \overline{\boldsymbol{t}}_2, \dots, \overline{\boldsymbol{t}}_d), \ \overline{\boldsymbol{T}}_{\overline{\boldsymbol{n}}} \overline{\boldsymbol{T}}_{\overline{\boldsymbol{n}}}^T = \overline{\boldsymbol{I}}_{d \times d}.$$

Furthermore we introduce the notation

$$\nabla_{\overline{\boldsymbol{n}}} p := \overline{\boldsymbol{T}}_{\overline{\boldsymbol{n}}}^T \nabla_{\overline{\boldsymbol{w}}} p, \ \overline{\boldsymbol{w}}_{\overline{\boldsymbol{n}}} := \overline{\boldsymbol{T}}_n^T \overline{\boldsymbol{w}}.$$

Then the characteristic polynomial corresponding to the determinant of the matrix $\boldsymbol{B}_n$ reads

$$|\boldsymbol{B}_{\overline{\boldsymbol{n}}}| = (-1)^{d+1} \left(\lambda - \frac{w_n}{w_{d+1} + p} \right)^{d-1} p_2(\lambda),$$

where the quadratic polynomial $p_2(\lambda) = \lambda^2 + \overline{p}\lambda + \overline{q}$ is determined by the coefficients

$$\overline{p} := \frac{w_n}{(w_{d+1} + p)^2} \sum_{i=1}^{d} \overline{w}_{\overline{t}_i} \partial_{t_i} p - \partial_{\overline{t}_1} p - \frac{2 w_n}{w_{d+1} + p},$$

$$\overline{q} := (1 + \partial_{w_{d+1}} p) \frac{w_n^2}{(w_{d+1} + p)^2} - \partial_{w_{d+1}} p - \frac{1}{w_{d+1} + p} \sum_{i=2}^{d} \overline{w}_{\overline{t}_i} \partial_{t_i} p.$$

The roots of the characteristic polynomial and, thus, the eigenvalues, are

$$\lambda_0 = \frac{w_n}{w_{d+1} + p} \ ((d-1)\text{-multiple}) \quad \text{or} \quad \lambda_\pm = -\frac{\overline{p}}{2} \pm \sqrt{\left(\frac{\overline{p}}{2}\right)^2 - \overline{q}}. \tag{B.6}$$

A system of linearly independent right eigenvectors is determined by

$$\boldsymbol{r}_0^i = \boldsymbol{t}_i - \alpha_i \left(\boldsymbol{e}_{d+1} + \lambda_0 \boldsymbol{t}_1 \right) \in \mathbb{R}^{d+1}, \ i = 2, \dots, d, \tag{B.7}$$

$$\boldsymbol{r}_\pm = \lambda_\pm \boldsymbol{t}_1 + \alpha_\pm \sum_{i=2}^{d} \overline{w}_{\overline{t}_i} \boldsymbol{t}_i + \boldsymbol{e}_{d+1} \in \mathbb{R}^{d+1} \tag{B.8}$$

with

$$\alpha_i := \frac{\partial_{\overline{t}_i} p}{\partial_{w_{d+1}} p + \lambda_0 \partial_{\overline{t}_1} p}, \qquad \alpha_\pm := \frac{w_{d+1} + p}{(w_{d+1} + p)^2 - w_n^2} \left(1 - \frac{w_n}{(w_{d+1} + p)} \lambda_\pm \right). \tag{B.9}$$

Here $\boldsymbol{t}_i = (\overline{\boldsymbol{t}}_i^T, 0)^T$ and $\boldsymbol{t}_1 = \boldsymbol{n} = (\overline{\boldsymbol{n}}^T, 0)^T$. The system of right eigenvectors is linearly independent, i.e., the matrix

$$\boldsymbol{R}_{\overline{n}} = (\boldsymbol{r}_-, \boldsymbol{r}_0^1, \dots, \boldsymbol{r}_0^{d-1}, \boldsymbol{r}_+)$$

is regular. Thus, a system of linearly independent left eigenvectors

$$\boldsymbol{L}_{\overline{n}} = (\boldsymbol{l}_-, \boldsymbol{l}_0^1, \dots, \boldsymbol{l}_0^{d-1}, \boldsymbol{l}_+)^T$$

exists that is orthogonal to the right eigenvectors, i.e.,

$$\boldsymbol{R}_{\overline{n}} \boldsymbol{L}_{\overline{n}} = \boldsymbol{I} \quad \text{and} \quad \boldsymbol{R}_{\overline{n}} \boldsymbol{A}_{\overline{n}} \boldsymbol{L}_{\overline{n}} = \boldsymbol{\Lambda}_{\overline{n}} := \text{diag}(\lambda_-, \lambda_0 \boldsymbol{1}_{d-1}^T, \lambda_+).$$

The system of orthogonal left eigenvectors is determined by

$$l_0^i = \frac{1}{D}\left(u_{\overline{t}_i}(\alpha_+ - \alpha_-)t_1 + \sum_{j=2}^{d}(D\delta_{i,j} - \alpha_j u_{\overline{t}_i}\beta)t_j - u_{\overline{t}_i}(\alpha_+\lambda_- - \alpha_-\lambda_+)e_{d+1}\right), \ i = 2, \dots, d, \tag{B.10}$$

$$l_\pm = \mp\frac{1}{D}\left((1 + \alpha_\mp S)t_1 + \sum_{i=2}^{d}\alpha_i(\lambda_0 - \lambda_\mp)t_i - (\alpha_\mp\lambda_0 S + \lambda_\mp)e_{d+1}\right) \tag{B.11}$$

with

$$D := \left(\lambda_- + \alpha_-\lambda_0 S\right)\left(1 + \alpha_+ S\right) - \left(\lambda_+ + \alpha_+\lambda_0 S\right)\left(1 + \alpha_- S\right), \ S := \sum_{i=2}^{d}\alpha_i u_{\overline{t}_i}, \tag{B.12}$$

$$\beta := \alpha_+(\lambda_- - \lambda_0) + \alpha_-(\lambda_0 - \lambda_+). \tag{B.13}$$

So far, we have not yet specified an equation of state. For this purpose we rewrite the conserved variables in terms of the primitive variables determined by the velocity $\overline{\boldsymbol{u}} := (u_1, \dots, u_d) \in \mathbb{R}^d$ and the pressure p, i.e.

$$w_i := 4p u_i\sqrt{1 + |\overline{\boldsymbol{u}}|^2}, \ i = 1, \dots, d \tag{B.14a}$$

$$w_{d+1} := p(3 + 4|\overline{\boldsymbol{u}}|^2). \tag{B.14b}$$

Reversely, the primitive variables can be rewritten in conserved variables as

$$u_i = \frac{w_i}{\sqrt{4p(w_{d+1} + p)}}, \ i = 1, \dots, d, \tag{B.15a}$$

$$p = \frac{1}{3}\left(-w_{d+1} + \sqrt{-3|\overline{\boldsymbol{w}}|^2 + 4w_{d+1}^2}\right) \geq 0. \tag{B.15b}$$

From this we determine the derivatives of the pressure by

$$\partial_{w_j}p = \begin{cases} -w_j/(w_{d+1} + 3p) & ,j = 1, \dots, d \\ (w_{d+1} - p)/(w_{d+1} + 3p) & ,j = d + 1 \end{cases}. \tag{B.16}$$

Introducing normal and tangential momentum $\overline{\boldsymbol{w}}_{\overline{n}} = (\overline{w}_{\overline{t}_1}, \dots, \overline{w}_{\overline{t}_d})^T$ and velocity $\overline{\boldsymbol{u}}_{\overline{n}} = (\overline{u}_{\overline{t}_1}, \dots, \overline{u}_{\overline{t}_d})^T$ by means of

$$\overline{\boldsymbol{w}}_{\overline{n}} := \overline{\boldsymbol{T}}_n^T \overline{\boldsymbol{w}} = 4p\overline{\boldsymbol{u}}_{\overline{n}}\sqrt{1 + |\overline{\boldsymbol{u}}|^2}, \ \overline{w}_{\overline{t}_i} = \boldsymbol{t}_i \cdot \overline{\boldsymbol{w}}, \quad \overline{w}_{\overline{t}_1} = \boldsymbol{t}_1 \cdot \overline{\boldsymbol{w}} \equiv \boldsymbol{n} \cdot \overline{\boldsymbol{w}} = w_n,$$

$$\overline{\boldsymbol{u}}_{\overline{n}} := \overline{\boldsymbol{T}}_n^T \overline{\boldsymbol{u}}, \ \overline{u}_{\overline{t}_i} = \boldsymbol{t}_i \cdot \overline{\boldsymbol{u}}, \quad \overline{u}_{\overline{t}_1} = \boldsymbol{t}_1 \cdot \overline{\boldsymbol{u}} \equiv \boldsymbol{n} \cdot \overline{\boldsymbol{u}} = u_n,$$

the pressure gradient and its directional derivatives in normal and tangential direction are determined by

$$\nabla_{\overline{w}}p = -\frac{\overline{\boldsymbol{w}}}{u_{d+1} + 3p} = -2\frac{\sqrt{1 + |\overline{\boldsymbol{u}}|^2}}{3 + 2|\overline{\boldsymbol{u}}|^2}\overline{\boldsymbol{u}}, \ \partial_{w_{d+1}}p = \frac{w_{d+1} - p}{w_{d+1} + 3p} = \frac{1 + 2|\overline{\boldsymbol{u}}|^2}{3 + 2|\overline{\boldsymbol{u}}|^2},$$

$$\nabla_{\overline{n}}p := \overline{\boldsymbol{T}}_n^T \nabla_{\overline{w}}p = -\frac{\overline{\boldsymbol{w}}_{\overline{n}}}{w_{d+1} + 3p} = -2\frac{\sqrt{1 + |\overline{\boldsymbol{u}}|^2}}{3 + 2|\overline{\boldsymbol{u}}|^2}\overline{\boldsymbol{u}}_{\overline{n}},$$

$$\partial_{t_i}p = \boldsymbol{t}_i \cdot \nabla_{\overline{w}}p = -\frac{\overline{w}_{\overline{t}_i}}{w_{d+1} + 3p} = -2\frac{\sqrt{1 + |\overline{\boldsymbol{u}}|^2}}{3 + 2|\overline{\boldsymbol{u}}|^2}\overline{u}_{\overline{t}_i}.$$

Then the eigenvalues in primitive variables read

$$\lambda_\pm = \frac{2u_n^2}{3 + 2|\overline{\boldsymbol{u}}|^2} \pm \frac{\sqrt{2(|\overline{\boldsymbol{u}}|^2 - u_n^2) + 3}}{3 + 2|\overline{\boldsymbol{u}}|^2}, \ \lambda_0 = \frac{u_n}{\sqrt{1 + |\overline{\boldsymbol{u}}|^2}}. \tag{B.17}$$

The left and right eigenvectors (B.11), (B.10) and (B.8), (B.7), respectively, can be written in primitive variables with

$$w_{\bar{u}_i} = 4p\bar{u}_{\bar{u}_i}\sqrt{1+|\overline{\boldsymbol{u}}|^2}, \ \alpha_i = -\frac{2\bar{u}_{\bar{u}_i}\sqrt{1+|\overline{\boldsymbol{u}}|^2}}{1+|\overline{\boldsymbol{u}}|^2+\sum_{i=2}^2(\bar{u}_{\bar{u}_i})^2}, \ i = 2,\dots,d,$$

$$\alpha_\pm = \frac{1}{4p\left(1+|\overline{\boldsymbol{u}}|^2-u_n^2\right)}\left(1-\frac{u_n}{\sqrt{1+|\overline{\boldsymbol{u}}|^2}}\lambda_\pm\right), \ S = \sum_{i=2}^d \alpha_i 4p\bar{u}_{\bar{u}_i}\sqrt{1+|\overline{\boldsymbol{u}}|^2}.$$

References

[1] M.A.E. Abdelrahman, M. Kunik, The ultra-relativistic Euler equations, Math. Methods Appl. Sci. 38 (7) (2015) 1247–1264.

[2] M.A.E. Abdelrahman, M. Kunik, A new front tracking scheme for the ultra-relativistic Euler equations, J. Comput. Phys. 275 (2014) 213–235.

[3] A. Bressan, Lecture notes on hyperbolic conservation laws, 1995.

[4] B. Cockburn, C.-W. Shu, Discontinuous Galerkin, slope limiters, Euler equations, Runge-Kutta, conservation laws, J. Comput. Phys. 141 (1998) 199–244.

[5] R. Courant, K.O. Friedrichs, Supersonic Flow and Shock Waves, Springer, New York, 1999.

[6] C.M. Dafermos, Hyperbolic Conservation Laws in Continuum Physics, Grundlehren der mathematischen Wissenschaften, vol. 325, Springer, Berlin, Heidelberg, 2010.

[7] H. Freistühler, Relativistic barotropic fluids: a Godunov-Boillat formulation for their dynamics and a discussion of two special classes, Arch. Ration. Mech. Anal. 232 (1) (2019) 473–488.

[8] N. Gerhard, F. Iacono, G. May, S. Müller, R. Schäfer, A high-order discontinuous Galerkin discretization with multiwavelet-based grid adaptation for compressible flows, J. Sci. Comput. 65 (1) (2015) 25–52.

[9] N. Gerhard, S. Müller, Adaptive multiresolution discontinuous Galerkin schemes for conservation laws: multi-dimensional case, Comput. Appl. Math. 35 (2) (2016) 321–349.

[10] N. Gerhard, S. Müller, A. Sikstel, A wavelet-free approach for multiresolution-based grid adaptation for conservation laws, Commun. Appl. Math. Comput. 4 (2021) 108–142.

[11] N. Hovhannisyan, S. Müller, R. Schäfer, Adaptive multiresolution discontinuous Galerkin schemes for conservation laws, Math. Comput. 285 (83) (2014) 113–151.

[12] H.K. Jenssen, On radially symmetric solutions to conservation laws. Nonlinear conservation laws and applications, IMA Vol. Math. Appl. 153 (2011) 331–351.

[13] M. Kunik, Selected Initial and Boundary Value Problems for Hyperbolic Systems and Kinetic Equations, Habilitation thesis, Otto-von-Guericke University Magdeburg, 2005, The thesis is available under https://opendata.uni-halle.de//handle/1981185920/30710.

[14] M. Kunik, H. Liu, G. Warnecke, Radially symmetric solutions of the ultra-relativistic Euler equations, Methods Appl. Anal. 28 (2021) 401–421.

[15] M. Kunik, S. Qamar, G. Warnecke, A BGK-type kinetic flux-vector splitting scheme for the ultra-relativistic Euler equations, SIAM J. Sci. Comput. 26 (1) (2004) 196–223.

[16] M. Kunik, S. Qamar, G. Warnecke, Second order accurate kinetic schemes for the ultra-relativistic Euler equations, J. Comput. Phys. 192 (2003) 695–726.

[17] M. Kunik, S. Qamar, G. Warnecke, Kinetic schemes for the ultra-relativistic Euler equations, J. Comput. Phys. 187 (2003) 572–596.

[18] G. Lai, Self-similar solutions of the radially symmetric relativistic Euler equations, Eur. J. Appl. Math. (2019) 1–31, https://doi.org/10.1017/S0956792519000317.

[19] O.A. Oleinik, Discontinuous solutions of nonlinear differential equations, Am. Math. Soc. Trans. Serv. 26 (1957) 95–172.

[20] T. Ruggeri, M. Sugiyama, Classical and Relativistic Rational Extended Thermodynamics of Gases, Springer, Cham, 2021.

[21] S. Weinberg, Gravitation and Cosmology, John Wiley, New York, 1972.